Climate Dynamics
https://doi.org/10.1007/s00382-024-07104-6

ORIGINAL ARTICLE

Thermodynamic characteristics of extreme heat waves over the middle and lower reaches of the Yangtze River Basin

Wencai Liu[1] · **Ning Shi**[1] · **Huijun Wang**[1,2,3] · **Qilei Huang**[1]

Received: 10 August 2023 / Accepted: 19 December 2023

Abstract
In August 2022, an exceptionally long-lasting heat wave (HW) affected the middle and lower reaches of the Yangtze River basin. This study uses the JRA55 daily reanalysis datasets to elucidate the thermodynamic characteristics of the daily evolution of historical extreme HWs in this region via the heat budget equation. HWs are generally characterized by the occurrence of anticyclonic circulation anomaly throughout the troposphere and positive air temperature anomaly with the maximum amplitude in the boundary layer. The anticyclonic anomaly can induce compression heating in the entire troposphere and warm zonal advection in the boundary layer. Meanwhile, due to the reduced cloud cover, more shortwave radiation reaches the ground surface, and the sensible heat flux becomes an important source of diabatic heating before the onset of HWs. The accumulated excessive heat in the HWs is primarily damped through the emission of longwave radiation and meridional thermal advection. For the HW in August 2022, its extreme persistence is mainly caused by prolonged adiabatic heating, enhanced diabatic heating during the developing stage and weakened diabatic cooling during the decay stage. The upper-level portion of the anticyclonic circulation anomalies is linked to the strengthened South Asia High. After applying the state-of-the-art dynamic metric, i.e., local finite wave activity, we reveal that the formation of the anomalous South Asia High in August 2022 is associated with the Stokes drift flux rather than the dispersion of Rossby wave energy. This characteristic sets it apart from other extreme HWs.

Keywords Heat wave · Yangtze River basin · Heat budget · Local finite amplitude wave activity

1 Introduction

In the summer of 2022, unprecedented and long-lasting extreme heat waves (HWs) attacked the Yangtze River basin (YRB) in China. These HWs resulted in severe droughts, wildfires and power shortages (Lu et al. 2023), causing great concerns among the public and posing a great challenge for scientists (Mallapaty 2022). Consequently, it is crucial to enhance research on the mechanisms behind HWs to effectively mitigate and prevent future disasters in the region.

Human-induced global warming is believed to significantly contribute to the increased frequency or intensity of HWs (e.g., Rahmstorf and Coumou 2011; Sun et al. 2016; Ma et al. 2017; Wang et al. 2020). According to linear statistical analysis for the period from 1979 onwards, some studies have suggested that the long-term warming trend may account for approximately 30% of the extreme hot summer in 2022 (e.g. He et al. 2023; Jiang et al. 2023; Liang et al. 2023; Wang et al. 2023). Interestingly, even when the long-term trend is removed, the summer of 2022 remains the hottest over the YRB (He et al. 2023; Jiang et al. 2023; Tang et al. 2023; Wang et al. 2023). Clearly, the summer of 2022 stands out from other extreme hot summers in the YRB. To gain a better understanding of HWs in the YRB, it is crucial to clarify the thermodynamics of extreme HWs in the summer of 2022 and compare them to other HWs.

A high-pressure circulation system is usually regarded as an essential factor for the occurrence of HWs (Xoplaki et al.

✉ Ning Shi
shining@nuist.edu.cn

[1] Collaborative Innovation Center on Forecast and Evaluation of Meteorological Disasters, School of Atmospheric Sciences, Nanjing University of Information Science and Technology, Nanjing, Jiangsu, China

[2] Southern Marine Science and Engineering Guangdong Laboratory (Zhuhai), Zhuhai, China

[3] Nansen-Zhu International Research Center, Institute of Atmospheric Physics, Chinese Academy of Sciences, Beijing, China

Published online: 14 February 2024

2003; Trigo 2005; Fischer et al. 2007; Horton et al. 2016; Wu et al. 2016; Hong et al. 2022). First, the subsidence of air masses associated with a high-pressure system can lead to local adiabatic compression heating. Second, the presence of a high-pressure system results in clear skies and increased solar radiation reaching the ground surface, which in turn leads to upward sensible heating flux from the ground surface. In East Asia, there are two high-pressure systems that can influence HWs in East Asia, i.e., the western Pacific subtropical high (WPSH) in the middle and lower troposphere and the South Asia high (SAH) in the upper troposphere/lower stratosphere (Sun et al. 2014; Li et al. 2015; Wang et al. 2016; Chen et al. 2019; Liu et al. 2019; Ren et al. 2020; Peng et al. 2023). The eastward expansion and strengthening of the SAH is often accompanied by the westward expansion of the WPSH. The overlap of these two high-pressure systems in East Asia enhances subsidence, creating favorable conditions for the formation of local HWs. In the summer of 2022, the overlap of these two high-pressure systems is evident over southeast China (e.g., Sun et al. 2023; Jiang et al. 2023; Tang et al. 2023).

From the perspective of atmospheric circulation, anomalously enhanced or displaced high-pressure systems are generally associated with some teleconnection patterns, e.g., the Pacific-Japan/East Asia–Pacific pattern (Nitta 1987; Huang 1992), Silk Road pattern (Lu et al. 2002; Ding and Wang 2005; Chen and Zhou 2018), and North Atlantic Oscillation (Sun 2012; Hong et al. 2022). These teleconnection patterns can influence the high-pressure systems over East Asia through the propagation of Rossby waves along the westerly jet-induced waveguide. For the extreme case in the summer of 2022, some studies have indicated that the propagation of Rossby waves is crucial for the persistence of anticyclonic anomalies over East Asia (e.g., Jiang et al. 2023; Wang et al. 2023; Tang et al. 2023). However, their results show that the wave-activity fluxes exhibit a noticeable divergence over the center of the anticyclonic anomalies, suggesting that the dispersion of Rossby wave energy actually plays a destructive rather than a constructive role. Therefore, further studies are needed to investigate the underlying mechanism behind the formation and persistence of anticyclonic anomalies over East Asia.

Various external forcing factors can contribute to the occurrence of HWs in China, such as snow cover (Wu et al. 2016), sea surface temperature anomalies over the Indian Ocean (Xie et al. 2016; He et al. 2023), North Pacific (Wang et al. 2000; Gao et al. 2018; Zhang et al. 2023) and North Atlantic (Sun 2014; Liu et al. 2019; Gao et al. 2018), condensation heat release over South Asia (Ding and Wang 2005; Tang et al. 2023; Wang et al. 2023) and multitimescale variability from external forcings (Liang et al. 2023). Additionally, soil−atmosphere feedback is considered to be another important factor (Fischer et al. 2007; Hirschi et al. 2011; Zhang and Wu 2011; Miralles et al. 2014; Wang et al 2016). As the temperature rises, a decrease in soil moisture can diminish the cooling effect of evapotranspiration, allowing the air temperature to further increase. Utilizing the linear regression method, Jiang et al. (2023) concluded that, in comparison to the sea surface temperature anomalies over the North Pacific and North Atlantic, soil−atmosphere feedback is the primary factor in the formation of extreme HWs over the YRB in 2022.

The aforementioned studies on the extreme summer of 2022 are mainly based on monthly or seasonal mean data. Some studies have noticed the month-to-month difference in the extreme HWs over the YRB in the summer of 2022. Specifically, the HWs in midsummer (July and August) were found to be the most severe (He et al. 2023; Tang et al. 2023). Due to the stronger soil−atmosphere feedback (Jiang et al. 2023) and the stronger anomalous anticyclone (Wang et al. 2023) in August, the HW is actually stronger in August than in July. Based on daily data, Liu et al. (2023) recently found that the HW in August 2022 is different from the two HWs in the early summer of 2022 in terms of the dominant frequency of the intraseasonal oscillation. Considering such an evident subseasonal variation in HWs, it is better to use daily data to delineate the formation mechanism of the HW in August 2022.

It is worth noting that within the thermodynamic framework, the soil−atmosphere feedback is diabatic heating, while the descending motion induced by the anomalous anticyclone may induce adiabatic heating. Liu et al. (2023) noted that the formation of the first two HWs in the early summer of 2022 is caused by adiabatic heating and subsequently by diabatic heating, while the one in the latter summer is associated with the adiabatic heating process. While many studies have highlighted the significance of both diabatic heating and adiabatic heating, the relative contribution of each remains uncertain. Furthermore, some studies have revealed that the advection and/or propagation of warm air from upstream regions also play a crucial role (Hong et al. 2022; Wang et al. 2023), although its impact may depend on the location (Horton et al. 2016; Zschenderlein et al. 2019; Röthlisberger and Papritz 2023). Thus, it is important to further investigate the relative contribution of horizontal thermal advection in the HWs over the YRB. The present study aims to address these concerns by analysing daily data.

The paper is organized as follows. Section 2 provides a description of the data and analysis methods used in this study. In Sect. 3, we address three questions: (1) What are the basic features of the daily thermodynamic process of

extreme HWs over the YRB? (2) What are the similarities and differences in the thermodynamics between the extreme HW in August 2022 and other extreme HWs? (3) What is the internal dynamic cause for the anticyclone anomalies in the middle and upper troposphere in August 2022? The final section presents a summary and discussion.

2 Materials and methods

A. Data

We use the daily Japanese 55-year Reanalysis dataset (JRA-55, Kobayashi et al. 2015) from 1958 to 2022 with a horizontal resolution of 1.25°. Four kinds of variables are utilized: (1) isobaric analysis fields, including air temperature, geopotential height, zonal wind velocity and vertical velocity, all of which are distributed over 37 pressure surfaces from 1000 to 1 hPa; (2) two-dimensional instantaneous diagnostic fields, including low cloud cover (1100–850 hPa), medium cloud cover (850–500 hPa) and high cloud cover (500–90 hPa); (3) two-dimensional average diagnostic fields, including the upward sensible heat flux at the ground surface, net downward shortwave radiation flux at the ground surface, net upward longwave radiation flux at the ground surface, and the upward longwave radiation flux at the top of atmosphere; and (4) surface analysis fields, i.e., air temperature at 2 m.

The present study focuses on the anomalies associated with extreme HWs. The daily anomaly field for a specific variable is obtained by subtracting the daily climatological mean over the period from 1958 to 2022 from the daily total field. To reduce the influence of the long-term trend associated with global warming, the linear trend in boreal summer during the entire period is removed. As done in Shi et al. (2019), all data are low-pass filtered by the Lanczos filtering procedure to isolate the 8-day slowly varying component, which helps mitigate the large daily variations in meteorological variables during extreme HWs. Unless otherwise stated, the anomalies mentioned later refer to the detrended 8-day low-frequency anomalies. The target season for this study is boreal summer from 1 June to 31 August.

b. Identification

Figure 1a illustrates the surface air temperature anomalies in the summer of 2022. Clearly, strong positive temperature anomalies (larger than 2 ℃) occur over a large region from the Mongolian Plateau southward to the Tibetan Plateau and further eastward to the middle and lower reaches of YRB. To circumvent the complexity of HW formation over high-altitude areas with complex terrain, the present study primarily focuses on the HWs in the middle and lower reaches of YRB, which are located in plain areas (dashed blue rectangle in Fig. 1). For the sake of brevity, the YRB will be

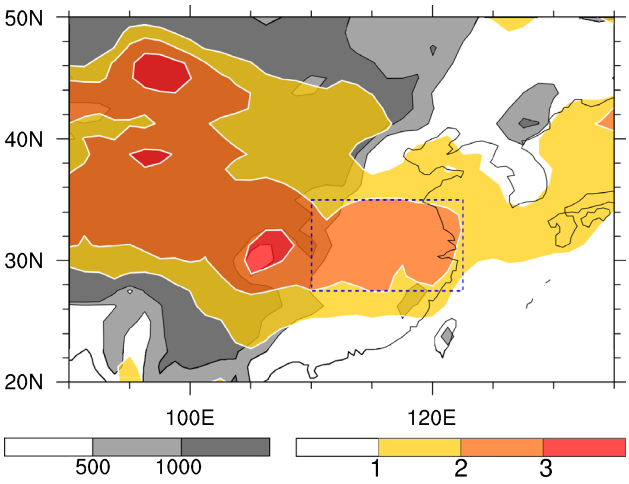

Fig. 1 Surface air temperature anomalies (color shading, units: ℃) in the summer (June–August) of 2022. Grey shading indicate the terrain height (units: m). Dashed blue rectangle represents the middle and lower reaches of the Yangtze River basin (YRB)

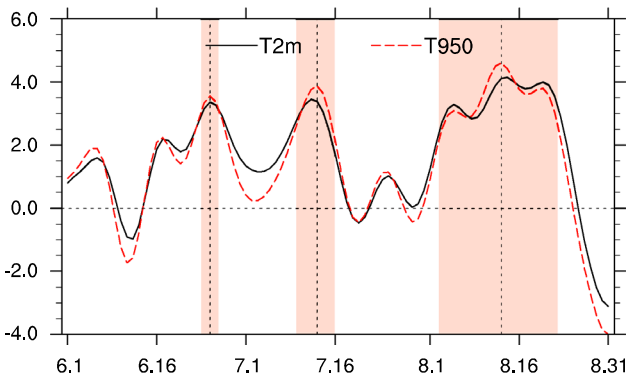

Fig. 2 Daily low-frequency surface air temperature anomalies and air temperature anomalies at 950 hPa averaged over the YRB during August 2022. The long-term trend has been removed for these two variables. Units are ℃. Pink shading indicates the periods for the three extreme heat waves (HWs), and vertical dashed lines indicate the peak day of the three events

referred to as its middle and lower reaches region throughout this paper. This region is densely populated, and HWs have a significant impact on human health, the economy, and ecosystems.

To analyse the temperature variation over the YRB as a whole, we take an area-average of air temperature over [27.5–35° N, 110–122.5° E] (blue dashed rectangle in Fig. 1). We use the detrended and low-pass-filtered air temperature anomalies at 950 hPa (T950) to identify the extreme HWs. Figure 2 shows the daily variations in area-averaged T950 anomalies and surface air temperature anomalies. Clearly, the two variables exhibit a similar variation, which

lends credence to the use of T950. Moreover, T950 is advantageous in thermodynamic diagnostic analysis because it simplifies the calculation of vertical differences compared to surface air temperature.

An extreme HW is identified based on three criteria. First, the amplitude of the area-averaged T950 for a particular day must exceed its local 95th percentile value. For a particular day, its local 95th percentile value is determined from a sequence of 31 days/year × 65 years = 2015 days. The 31-day segment of each year is centered at the particular calendar day. Second, the duration of an extreme HW is not shorter than 3 days. Last, the interval between every two extreme HWs must be larger than 8 days to ensure the independence of each case in the following composite analysis.

c. Thermodynamic budget equation

As in Shi et al. (2020), we employ the anomalous heat budget equation:

$$\underbrace{\frac{\partial T'}{\partial t}}_{dt} = \underbrace{-\left(u\frac{\partial T}{\partial x}\right)'}_{ut} \underbrace{-\left(v\frac{\partial T}{\partial y}\right)'}_{vt} \underbrace{-\left(\omega\frac{\partial T}{\partial p} - \frac{RT\omega}{C_p p}\right)'}_{wt} \underbrace{+\frac{Q'}{C_p}}_{dia}, \quad (1)$$

The prime symbol indicates the daily anomaly with respect to the local daily climatological mean. The terms u, v, and ω represent the velocity on isobaric surfaces. C_p is the specific heat at constant pressure, and R is the gas constant of dry air. Q/C_p is the rate of diabatic heating per unit mass, which is estimated as the residual of the thermodynamic equation. The terms of Eq. (1) from left to right represent (i) the observed tendency of the air temperature anomaly, (ii) the anomalous thermal advection in the zonal direction and (iii) that in the meridional direction, (iv) the contribution from the vertical motions, which includes the anomalous vertical thermal advection and compression, and (v) the anomalous diabatic heating. These terms are denoted *dt*, *ut*, *vt*, *wt*, and *dia*, respectively. The diagnostic equation allows for a straightforward measurement of the relative importance of each thermal process. Note that the anomalies of each term in Eq. (1) are also detrended and low-pass-filtered.

2.1 d. Local finite-amplitude wave activity

Recently, Huang and Nakamura (2016) proposed a state-of-the-art dynamic metric, i.e., local finite-amplitude wave activity (LWA), from the potential vorticity perspective, which is quite suitable for measuring the waviness of circulation. The LWA and its budget equation are defined on isobaric surfaces in spherical coordinates as follows:

$$\begin{cases} A = \dfrac{a}{\cos\phi}\displaystyle\int_0^{\Delta_\varphi} q_e(\lambda,\varphi,\varphi',z,t)\cos(\varphi+\varphi')d\varphi' \\ \underbrace{\dfrac{\partial A\cos\varphi}{\partial t}}_{\text{LWA tendency}} = -\underbrace{\dfrac{1}{a\cos\varphi}\dfrac{\partial F}{\partial\lambda}}_{\text{convergence of zonal LWA flux}} \underbrace{-\cos\varphi v_e q_e\big|_{\varphi'=0}}_{\text{convergence of zonal LWA flux}} + residual \\ F_\lambda = \underbrace{u_{\mathrm{REF}}A\cos\varphi}_{F_1} \underbrace{-a\displaystyle\int_0^{\Delta_\varphi} u_e q_e\cos(\varphi+\varphi')d\varphi'}_{F_2} \end{cases} \quad (2)$$

A is the LWA. q is the quasigeostrophic potential vorticity, $z = -H\ \mathrm{ln}(z - z_0)$ is the pressure pseudoheight ($p_0 = 1000$ hPa), $H \approx 7$ km is the scale height, and a is the radius of Earth. $(q_e, u_e, v_e, \theta_e)$ are departures from the wave-free reference state $(q_{\mathrm{REF}}, u_{\mathrm{REF}}, v_{\mathrm{REF}}, \theta_{\mathrm{REF}})$. q_{REF} is obtained by "zonalizing" the instantaneous quasigeostrophic potential vorticity contours through an area-preserving map. $v_{\mathrm{REF}} = 0$ and $(u_{\mathrm{REF}}, \theta_{\mathrm{REF}})$ can be further solved through the thermal wind balance. φ' is the latitudinal displacement from equivalent latitude φ, and $\Delta\varphi(\lambda,\varphi,z,t)$ is the meridional displacement of the quasigeostrophic potential vorticity contour $q = q_{\mathrm{REF}}$ from φ. The *residual* term in the second equation consists of (a) diabatic heating effects, (b) nonconservative sources/sinks of the LWA, e.g., dissipation through mixing or wave breaking and radiative and Ekman damping, and (c) inevitable analysis errors, e.g., sampling errors, nonquasigeostrophic effects, and truncation errors. More details on the calculation can be found in the Supplemental Material of the present study or the supporting information sections of Huang and Nakamura (2017).

Dynamically, the positive value of F_1 (F_2) means the eastward transportation of the LWA by u_{REF} (u_e). F_2 represents the Stokes drift flux, which is the nonlinear modification of the flux by eddies. In Sect. 3, we show that the convergence of F_2 contributes the most to the formation of anticyclonic anomalies over East Asia. This result is similar to Nakamura and Huang (2018), in which F_2 is regarded as having an important role in the formation of eddies with finite amplitudes (such as blocking). Unless otherwise stated, we do not transform the term $-\cos\varphi v_e q_e\big|_{\varphi'=0}$ in Eq. (2) into the convergence of the generalized 3-dimensional E-P flux. For simplicity, $-\cos\varphi v_e q_e\big|_{\varphi'=0}$ is referred to as $-v_e q_e$ in the following text.

3 Results

A. Circulation anomalies

According to the identification method of HWs introduced in Sect. 2b, a total of 49 extreme HWs in the YRB are identified (Table S1 of Supplemental Material). HWs

occur once a month during the three summer months of 2022 (pink shading). It is worth noting that the HW in August 2022 lasted from August 3rd to August 22nd, making it the longest-lasting event in the past 65 years, surpassing the second longest event in 2013 by 7 days. For simplicity, we will refer to this extremely long-lived HW in August 2022 as the Aug2022 case in the following text. To extract the common features for the HWs, a composite analysis is conducted on the 48 cases with a duration ranging from 3 to 13 days. Additionally, an attempt was made to classify the 48 cases into two groups: the short-lived group (3–5 days) and the medium-lived group (6–13 days). However, the results showed no fundamental difference between these two subsets, except for the longer duration of the medium-lived group (not shown). Therefore, we combined the short-lived and medium-lived groups into one group and referred to it as ordinary HWs.

Figure 3 shows the vertical cross-section of circulation anomalies along 30°N for ordinary HWs (left column) and the Aug2022 case (right column). These anomalies are averaged over the entire lifecycle for each case before applying the composite procedure. For ordinary HWs, positive air temperature anomalies are observed over the YRB and the surrounding regions throughout the troposphere, with the highest amplitude near the ground surface (Fig. 3a). Additionally, a notable significant positive height anomaly is observed throughout the troposphere and lower stratosphere, with its center at approximately 150 hPa (Fig. 3e). Figure 3g shows the composite geopotential height anomalies at 150 hPa and the horizontal wind velocity at 950 hPa. The height anomalies at 500 hPa (not shown) exhibit a similar pattern to those at 150 hPa, indicating a quasi-barotropic structure in the middle and upper troposphere (Fig. 3e). The primary significant anticyclonic height anomalies are centered over East Asia and merge with those over the northwestern Pacific (Fig. 3g). However, the anticyclonic circulation anomalies over East Asia shift further southward in the lower troposphere, forming a northward-tilted structure over East Asia. The YRB is subject to the influence of the southwesterlies in the lower troposphere. In fact, such anticyclonic anomalies result from a combination of the enhanced SAH in the upper troposphere and the westward extension of the WPSH in the middle-to-lower troposphere (e.g., Jiang et al. 2023; Peng et al. 2023; Sun et al. 2023; Tang et al. 2023). Beneath the center of the anticyclonic anomalies, significant subsidence dominates throughout the troposphere (Fig. 3c). Subsidence in the upper troposphere can induce the accumulation of air masses and further facilitate the westward extension of the WPSH in the middle and lower troposphere.

In the Aug2022 case, the circulation anomalies exhibit similarities to those of ordinary HWs. For instance, there are positive air temperature anomalies throughout the troposphere (Fig. 3b), accompanied by significant anticyclonic height anomalies (Fig. 3f) and predominant descending motion (Fig. 3d). Moreover, both the upper-layer and the lower-layer anticyclonic anomalies overlap over East Asia with a northward-tilted structure (Fig. 3h). Hence, the fundamental circulation anomalies of extreme HWs remain unchanged in the Aug2022 case. The main difference lies in the increased persistence of the typical circulation anomalies.

b. Thermodynamic features

Figure 4 presents the daily variation in each term of the thermodynamic budget equation (Eq. 2), which is area-averaged over the YRB on different isobaric surfaces. Since the boundary layer process may be involved in HWs (Miralles et al. 2014), we discuss the thermodynamic processes in the boundary layer and free atmosphere separately. As JRA55 does not provide boundary layer height data, we use the planetary boundary height field from the ERA5 monthly datasets instead (Hersbach et al. 2020). In August 2022, the planetary boundary height in the YRB is approximately 580 m, while the August climatological mean is 467 m. The mean terrain height is approximately 232 m. Therefore, the sum of 232 m and 580 m equals 812 m for August 2022. According to the 1976 U.S. standard atmosphere, this height corresponds to 919 hPa, which is calculated using the function *stdatmus_z2tdp* of NCL (https://www.ncl.ucar.edu/Document/Functions/Built-in/stdatmus_p2tdz.shtml). Hence, in the present study, the portions above and below 900 hPa are roughly considered the free atmosphere and the planetary boundary layer, respectively.

For ordinary HWs, the air temperature in the lower troposphere exhibits a clear positive tendency anomaly *dt* from day – 6 to day 0, followed by a negative tendency from day 1 to 6, indicating the accumulation and release of excessive heat, respectively (black lines in Figs. 4a, c, e and g). Here, day 0 means the peak day, and day N (-N) represents the N day after (before) the peak day. The average start day and end day of the 48 ordinary HWs are day – 2.3 and day 2.3, respectively. They are indicated by vertical black solid lines in Fig. 4 for ease of discussion. In the middle and upper troposphere, the temperature tendency anomaly is not as pronounced (Fig. S1a, c), which aligns with the smaller amplitude of the air temperature anomalies (Fig. 3a).

The descending motion shown in Fig. 3c induces significant adiabatic heating *wt* with the maximum amplitude at approximately day – 1 in the lower troposphere (purple lines in the left column of Fig. 4). This adiabatic heating is the main contributor to the positive *dt* anomaly before the onset of HWs in the free atmosphere (e.g., 850 hPa and 900 hPa, and 300 hPa and 500 hPa shown in Fig. S1). In fact, *wt* mainly arises from the compression $R(T\omega)'/C_pP$ (not shown). In the middle and upper troposphere, the heat budget is characterized by a balance to a great extent between adiabatic heating *wt* and diabatic cooling *dia* (Fig. S1). Note

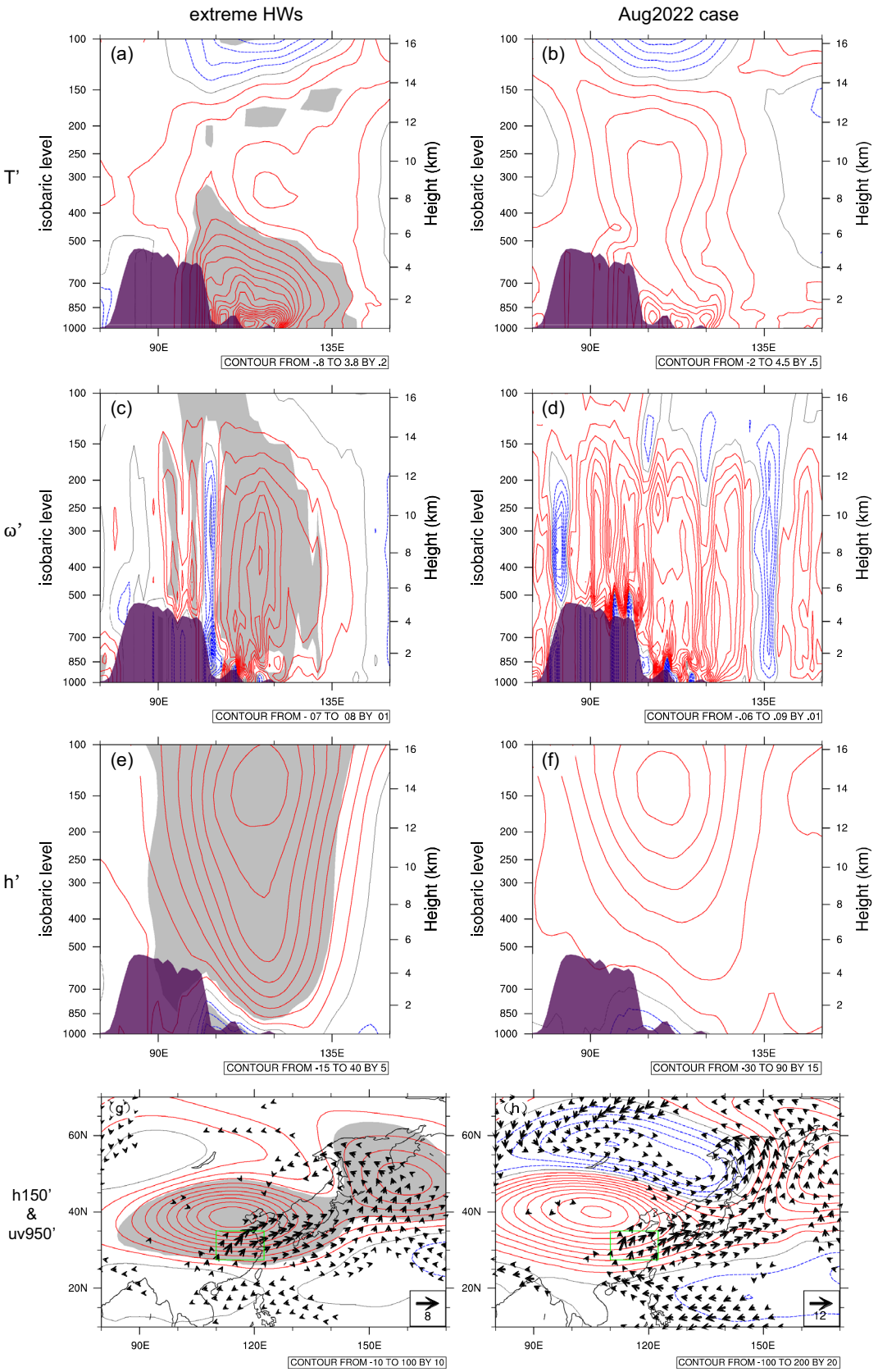
extreme HWs
Aug2022 case
T'
ω'
h'
h150'
&
uv950'
(a)
(b)
(c)
(d)
(e)
(f)
(g)
(h)
isobaric level
Height (km)
90E
135E
120E
150E
60N
40N
20N
CONTOUR FROM -.8 TO 3.8 BY .2
CONTOUR FROM -2 TO 4.5 BY .5
CONTOUR FROM - 07 TO 08 BY 01
CONTOUR FROM -.06 TO .09 BY .01
CONTOUR FROM -15 TO 40 BY 5
CONTOUR FROM -30 TO 90 BY 15
CONTOUR FROM -10 TO 100 BY 10
CONTOUR FROM -100 TO 200 BY 20

◂**Fig. 3** Mean circulation anomalies for extreme HWs which is averaged over their lifecycle. Left column is the composite results for ordinary HWs, right column is for the Aug2022 case. The first three rows show the vertical cross section along 30°N of air temperature anomalies (units: ℃), omega anomalies (units: Pa/s) and geopotential anomalies (units: gpm), respectively. Purple shading represent terrain. The last row shows the composite geopotential height at 150 hPa (contour, units: gpm) and wind velocity at 950 hPa (vector, units: m/s). Wind speed less than 1 m/s and 2 m/s are omitted in (**g**, **h**), respectively. In (**g**, **h**), green rectangle represents the YRB. Red solid lines indicate the positive anomalies, blue dashed line the negative anomalies, and black lines are the zero contours. Contour range and intervals are indicated in the bottom-right corner of each panel. Grey shading represent the significance at the 95% confidence level

that the relative importance of *wt* decreases in the boundary layer. The zonal thermal advection *ut* becomes evident and even comparable to *wt* in the boundary layer (Fig. 4e, g) from approximately day – 5 to day 2. In addition, *dia* has a significant maximum positive value of 0.3 K/day at approximately day – 4 in the boundary layer. This indicates that in the boundary layer, the HWs are generally initiated by diabatic heating and maintained by adiabatic heating due to subsidence *wt* and zonal thermal advection *ut*. As the air temperature rises, the positive temperature anomalies are gradually offset by the significant anomalous cooling effect from the meridional thermal advection *vt* and diabatic heating *dia* after day – 1. The reason why *dia* changes from heating before the start day to cooling after the start day will be further explored in the next subsection. In fact, both the anomalous adiabatic heating effect *ut* and adiabatic cooling effect *vt* in the lower troposphere are associated with the anomalous westward extension of the WPSH (Fig. 3g). Thus, the anticyclonic anomalies over East Asia and the western Pacific play a two-faceted role in the formation and maintenance of HWs over the YRB.

In the Aug2022 case, there are three warming periods in the lower troposphere, i.e., day – 14 to day – 6, day – 5 to day 0 and day 5–7 (black lines in the right column of Fig. 4). Overall, the thermodynamics of the Aug2022 case closely resemble those of ordinary HWs. For instance, at 850 hPa and 900 hPa, the positive temperature tendency anomaly is mainly due to adiabatic heating *wt,* with zonal thermal advection *ut* playing a secondary role. In the boundary layer, the case is triggered by *dia* (from day – 15 to – 10), sustained by two adiabatic processes (*wt* and *ut*), and weakened by *vt*. Therefore, the two-facet role played directly by the anticyclonic anomalies is still evident in the Aug2022 case. However, there are two aspects where the thermodynamics of the Aug2022 case differ from ordinary HWs. First, in the free atmosphere, the positive anomalies of both *wt* and *ut* persist for a longer period, and they are counteracted by the prolonged cooling effect through *vt* and *dia*. Second, in the boundary layer, *dia* exhibits an evident positive anomaly before day 0, but does not exhibit an evident negative anomaly afterwards except for the period from day 0 to 4. Thus, the enhanced diabatic heating during the developing stage and the prolonged adiabatic heating, along with the weakened diabatic cooling during the decay stage, explains the extreme persistence of the Aug2022 case in the boundary layer.

c. Sources of diabatic heating

We further investigate the factors contributing to diabatic heating. The presence of an anomalously enhanced anticyclonic circulation (Fig. 3) is often accompanied by clear skies. As seen in Fig. 5a, ordinary HWs exhibit significantly less low, medium, and high cloud cover from approximately day – 5 to 4. Note that the high clouds primarily consist of ice crystals. It is widely accepted that high cloud cover has a greater impact on longwave radiation than shortwave radiation. Consistent with the less low and medium cloud cover, more solar radiation reaches the Earth's surface (Fig. 5b). Subsequently, the warmed ground can heat the air masses aloft through a significant positive upward sensible heat flux (Fig. 5c). These sensible heat flux anomalies contribute to the positive diabatic heating anomalies and the observed positive *dt* anomalies at days – 5 and – 4 (Fig. 4e, g). These findings align with previous studies on extreme HWs in East Asia, which were based on monthly mean datasets. (e.g., Wu et al. 2016; Hong et al. 2022). Although the net upward longwave radiation flux anomaly at the ground surface is positive (Fig. S2a), the warmed air masses also lose heat by emitting longwave radiation. To measure the net longwave radiation flux absorbed by the air masses, we calculate the net column longwave radiation flux by subtracting the upward longwave radiation flux at the top of the atmosphere from the net upward longwave radiation flux at the ground surface. A positive (negative) value means a net income (loss) of longwave radiation flux for the column air masses. Figure 5d shows that for ordinary HWs, the net column longwave radiation flux anomaly is negative from day – 6 to 4, with the maximum amplitude occurring on day – 1. This indicates that the air masses are gradually cooled by emitting longwave radiation, which is consistent with the maximum diabatic cooling around day 0 (left column of Figs. 4 and S1).

Regarding the Aug2022 case (red lines in Fig. 5), there is also less low and medium cloud cover, allowing more net shortwave radiation to reach the ground surface before day 12. This behavior is similar to that of ordinary HWs, except for the longer persistence. However, the upward sensible heat flux does not show a consistent variation with that of the shortwave radiation flux. For instance, around day – 14, the sensible heat flux anomaly achieves its maximum positive value, while the positive shortwave radiation flux anomaly achieves its minimum value. It is possible that the soil-atmospheric feedback process (Fischer et al. 2007; Hirschi et al. 2011; Zhang and Wu 2011; Miralles

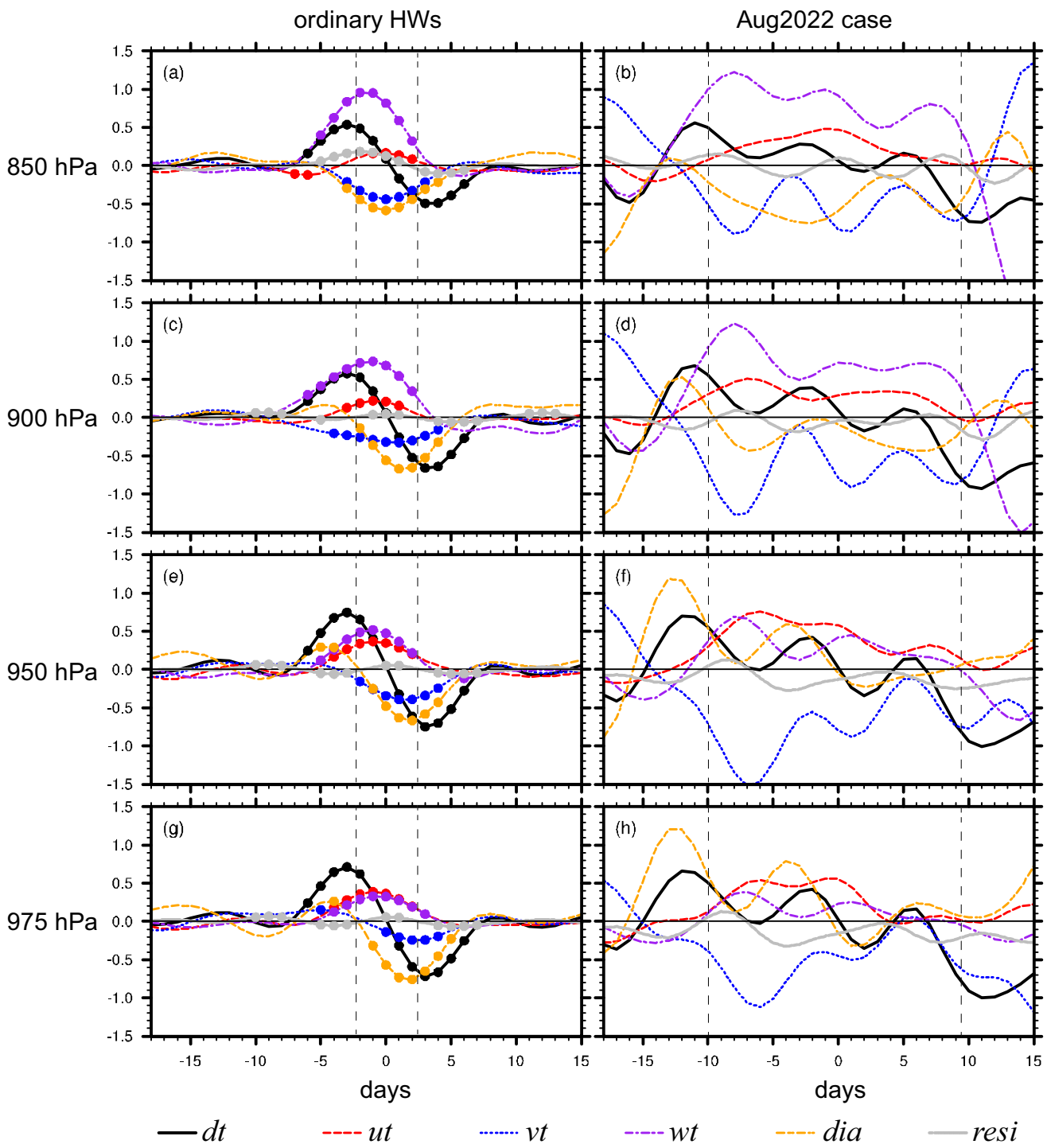

Fig. 4 Daily variation of the area-averaged anomalies of the thermodynamic budget terms for the extreme HWs in the YRB. Units: ℃. Left column is for ordinary HWs, and right column for the Aug2022 case. Rows from the upper to bottom are at 850 hPa, 900 hPa, 950 hPa and 975 hPa, respectively. Day 0 means the peak day of the HWs. The vertical dashed black lines in the left column represent the averaged start day and end day of ordinary HWs, and the ones in the right column represent the start day and end day of Aug2022 case

et al. 2014; Jiang et al. 2023) amplifies the sensible heating flux from day – 15 to day – 10. This aspect falls beyond the scope of the present study. At least, it can be concluded that the sensible heating flux is an important source for diabatic heating until day – 2 (Figs. 4f, 4h and 5c). The net column longwave radiation flux typically reaches its

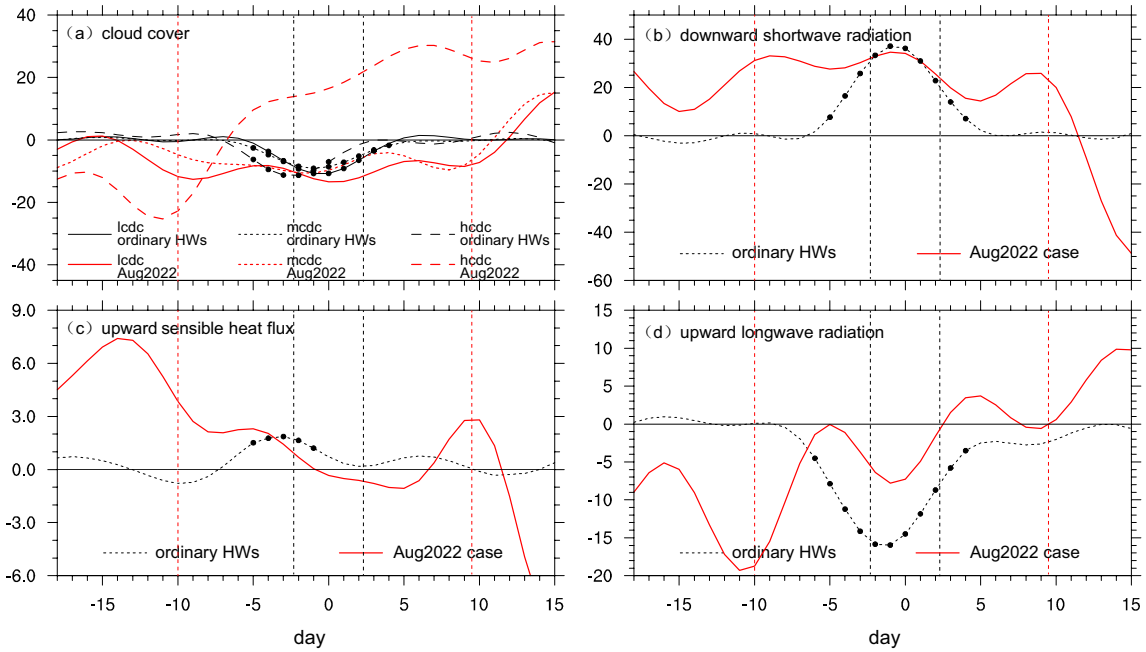

Fig. 5 **a** Cloud cover anomalies (units: %) for ordinary HWs (black lines) and the Aug2022 case (red lines). The variables are area-averaged over the YRB. Solid lines are for low cloud cover, dotted lines medium cloud cover and dashed lines high cloud cover. Black filled circles represent the significance at 95% confidence level. **b** As in **a**, but for net downward shortwave radiation flux at the ground surface (units: W/m^{-2}). **c** As in **b**, but for the upward sensible heat flux at the ground surface (units: W/m^{-2}). **d** As in **c**, but for the net upward longwave radiation flux for the column air (units: W/m^{-2}). The vertical dashed red and black lines represent the averaged start day and end day of ordinary HWs and the start day and end day of Aug2022 case, respectively

maximum negative value on day – 9 (Fig. 5d), which is one day after the maximum temperature tendency anomaly *dt* (Figs. 4f and h). This confirms that the warmed air masses are cooled down through the emission of longwave radiation in the Aug2022 case, similar to ordinary HWs. However, the Aug2022 case exhibits a new characteristic. The anomaly in the net column longwave radiation flux shows an increasing trend after day – 11, which aligns with the variation in high cloud cover on the whole (Fig. 5a). This suggests that the increased anomaly in high cloud cover contributes to trapping more longwave radiation. Consequently, unlike ordinary HWs, the diabatic heating *dia* in the Aug2022 case does not display a significant negative anomaly after the start day (Figs. 4f and h), allowing for the accumulation of heat and its persistence. Condensation heating may have a positive impact on the formation of the Aug2022 case only on approximately day 2 and day 3, which is implied by the evident positive precipitation anomalies over the YRB (Fig. S2b).

Overall, sensible heating at the ground surface is an important source of diabatic heating that initiates HWs over the YRB. As the air masses gradually warm up, they release heat through emitting longwave radiation, which becomes an important source for the evident diabatic cooling after the onset of HWs. However, in the case of Aug2022, the high clouds appear to trap longwave radiation, resulting in a slowdown of the cooling process.

d. Dynamics for anomalous SAH

The previous sections have discussed how the anticyclonic circulation anomaly can impact the formation of HWs. The impact can occur directly through the adiabatic process and indirectly through the diabatic process. It is important to further investigate the formation mechanism of this anticyclonic circulation anomaly. The anticyclonic circulation anomaly throughout the troposphere (Fig. 3e, f) corresponds to the enhanced SAH in the upper troposphere/lower stratosphere and the weakened low pressure circulation over Asia in the middle and lower troposphere. Note that the weakened low pressure circulation will reduce the difference in pressure or height field between it and the subtropical highs to its east and west, forming a more uniform circulation in the subtropical region. Therefore, the waviness will be enhanced in the upper troposphere but reduced in the lower troposphere. It corresponds to the evident positive LWA anomaly in the upper troposphere/lower stratosphere, with the maximum amplitude occurring at approximately 10 km for both ordinary HWs and the Aug2022 case (Fig. 6). In the following discussion, each term of the LWA budget equation (Eq. 2) is averaged vertically from 7 to 17 km with a weight of air density, i.e., $\langle(\cdot)\rangle = \int_{7\mathrm{km}}^{17\mathrm{km}} e^{-z/H}(\cdot)dz/H$.

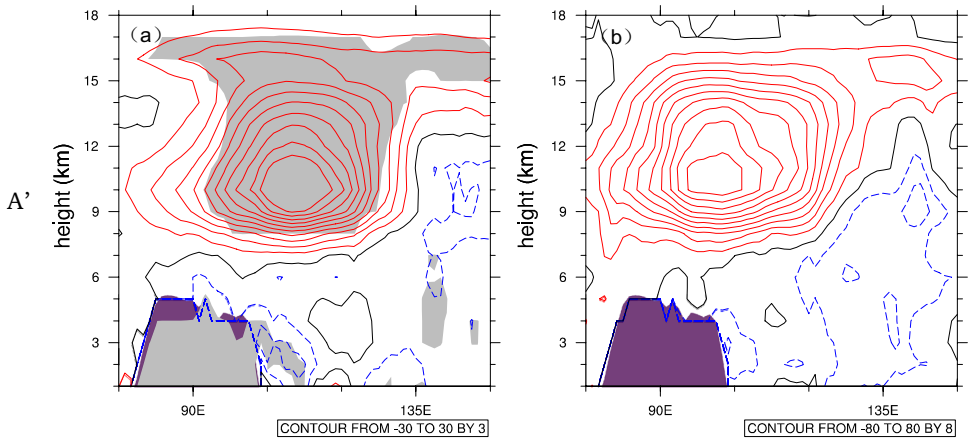

Fig. 6 Same as Fig. 3a, but for the composite LWA anomalies (Units: m/s). **a** Ordinary HWs. **b** Aug2022 case

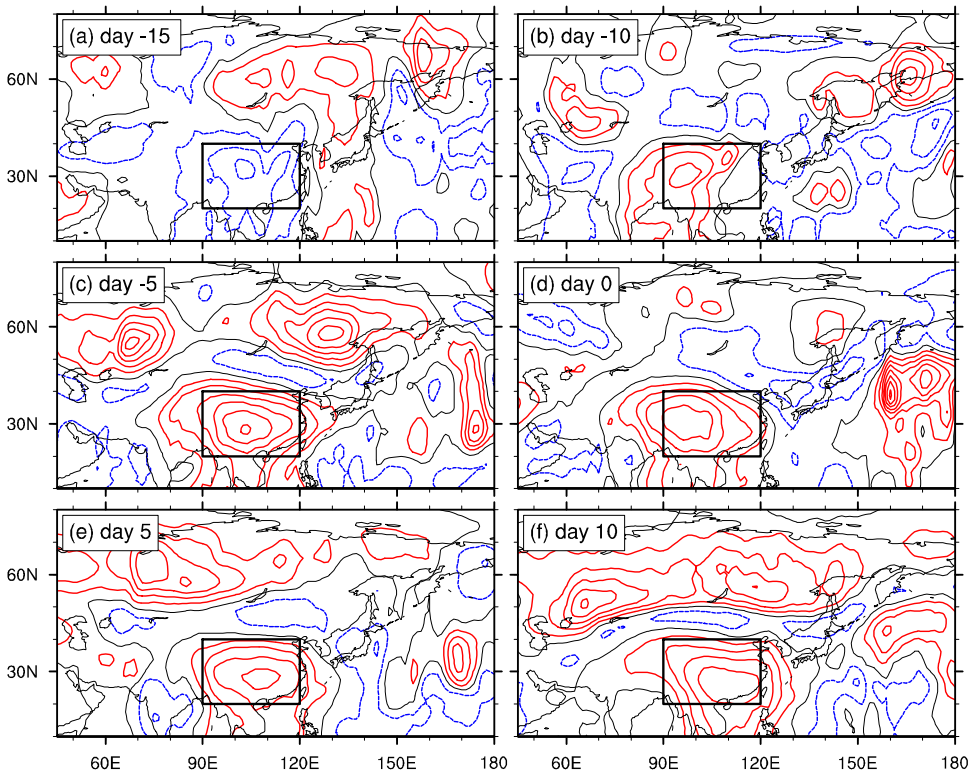

Fig. 7 Evolution of the column-averaged LWA anomalies (m/s) in the upper troposphere/lower stratosphere which is from 7 to 17 km for the extreme HWs over the YRB in August 2022. Red solid contours represent the positive values, blue dashed contours the negative values, and thin black solid line the zero lines. Contour interval is 10 m/s. The black rectangle represents the eastern China where the area-average is taken for the diagnostic of LWA anomalies

Figure 7 shows the evolution of column-averaged LWA anomalies for the Aug2022 case. On day – 15, negative LWA anomalies are observed over eastern China, suggesting a weakened SAH. However, these anomalies become positive on day – 10 and persist until day 10. In fact, significant LWA anomalies also occur over eastern China during ordinary HWs but are only significant from day – 5 to day 3 (not shown). To analyse the evolution of the LWA anomalies over eastern China, we calculate the column average for each term of Eq. (2) over the region [20-40°N, 90-120°E]. For ordinary HWs, the column-averaged LWA experiences a significant enhancement from day – 6 to day – 2 and weakens from day 1 to 4 (Fig. 8a). This enhancement of the LWA mainly results from the meridional potential vorticity flux $-v_e q_e$, indicating that the accumulation of Rossby wave energy plays a positive role in the formation of positive LWA anomalies. This dynamic feature has been emphasized in many other studies (e.g., Jiang et al. 2023; Wang et al. 2023; Tang et al. 2023). After day 0, the positive LWA anomalies are diminished due to the divergence of F_1+F_2 and diabatic heating effects.

For the Aug 2022 case (Fig. 8b), the LWA experiences evident enhancement from day – 15 to day – 6. During this period, in sharp contrast, the convergence of F_2 stands out as the main contributor to the enhancement of the LWA. In fact, the convergence of F_2 also positively contributes to the

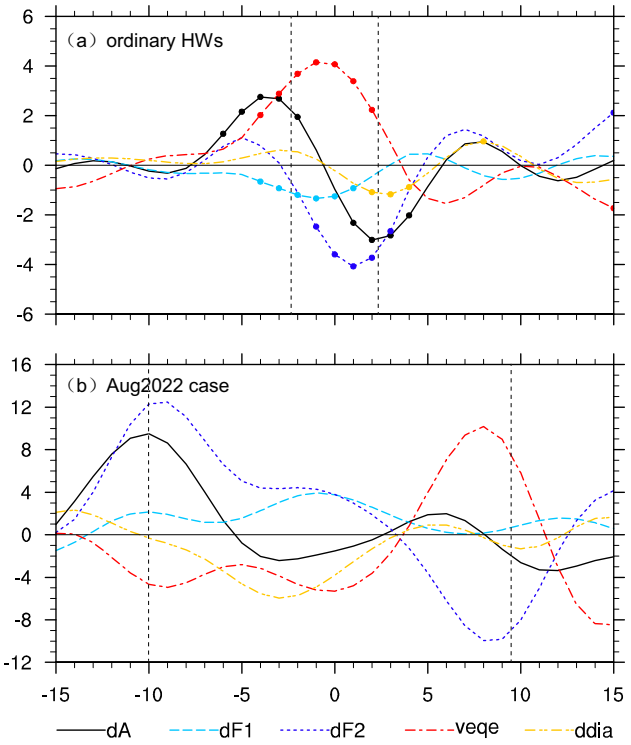

Fig. 8 Daily evolution of column-integrated LWA budget terms (m/s) for the extreme HWs over eastern China. **a** Ordinary HWs, **b** Aug2022 case. Each term is area-averaged over the eastern China [20–40° N, 90–120° E] which is indicated by the black rectangle in Fig. 6

enhancement of the LWA for ordinary HWs around day – 5 but lacks significance (Fig. 8a). The meridional potential vorticity flux $-v_e q_e$ anomaly in the Aug2022 case actually has a negative sign, indicating a divergence of Rossby wave energy. Thus, it is actually unfavorable for the maintenance of the enhanced SAH. The $-v_e q_e$ anomaly becomes positive only during the period from day 5 to day 11. Fig. S3 shows the three components of $-v_e q_e$ for both the ordinary HWs and the Aug2022 case. All three components basically show a synchronous variation with $-v_e q_e$. Clearly, the formation mechanism of the anomalous SAH in the Aug2022 case differs from that of ordinary HWs.

Overall, the formation of the anomalous SAH in the Aug 2022 case involves some new dynamics, with the nonlinear effect (convergence of F_2) playing a predominant role in its enhancement, while $-v_e q_e$ mainly counteract the maintenance of the anomalous SAH. The reason behind the strong convergence of the Stokes drift flux in the Aug2022 case remains a topic for future studies.

4 Conclusion and discussion

A. Conclusion

The present study explores the thermodynamics of HWs over the YRB based on the JRA55 daily reanalysis datasets. A comparative analysis is conducted to elucidate the similarities and differences in the thermodynamic characteristics between ordinary HWs and the Aug2022 case. Here, ordinary HWs are defined as those lasting between 3 and 14 days, while the Aug2022 case has an unusually long duration of 20 days.

Both ordinary HWs and the Aug2022 case are characterized by the appearance of anticyclonic circulation anomaly throughout the troposphere and lower stratosphere and positive air temperature anomalies with the maximum amplitude in the boundary layer. The anticyclonic anomaly can affect air temperature through both adiabatic and diabatic processes. The anticyclonic anomaly is accompanied by evident descent motion anomalies that prevail in the troposphere. The induced adiabatic compression heating serves as the primary adiabatic heating source in the entire troposphere. In the boundary layer, eastward warm advection is also evident, which corresponds to the westward extension of the WPSH. In addition, the anticyclonic circulation anomaly leads to reduced low and medium cloud cover and increased shortwave radiation reaching the ground. Consequently, the sensible heating flux is enhanced, becoming an important diabatic heating source prior to the onset of HWs. HWs gradually form due to the combined heating effect of descent motion, zonal thermal advection, and diabatic heating. As the air temperature increases, it is gradually cooled by emission of longwave radiation flux and meridional thermal advection.

In the extreme Aug2022 case, the above-mentioned thermal processes also occur, but they last for longer durations. Note that the cooling effect due to the emission of longwave radiation gradually diminishes during the evolution of the Aug2022 case and even acts as a heating source after day 2, which might be associated the trapping effect of the high clouds on longwave radiation. Therefore, consistent with the persistent anticyclonic circulation anomalies, the enhanced diabatic heating process during the developing stage and prolonged adiabatic heating processes (i.e., *ut* and *wt*) during the whole lifecycle, combined with the weakened diabatic cooling effect during the decay stage, accounts for the unusually long duration of the Aug2022 case.

The anticyclonic circulation anomalies are analysed using a state-of-the-art dynamic metric called the LWA. The analysis reveals significant positive LWA anomalies in the upper troposphere and lower stratosphere over eastern China, corresponding to the enhanced SAH. Through the LWA budget equation, we demonstrate that the enhanced SAH in the Aug2022 case is primarily caused by the nonlinear effect (i.e., the Stokes drift flux). The dispersion of Rossby wave energy plays a destructive role in the enhanced SAH, except for the last 5 days of the Aug2022 case. Therefore, the

Table 1 Numbers of extreme HWs and extreme LWA events over eastern China during different periods

period	Extreme HWs	Extreme SAH events	Numbers of overlapped events
1958–1969 (12 year)	12	13	3
1970–1979 (10 year)	6	14	4
1980–1989 (10 year)	7	5	1
1990–1999 (10 year)	3	4	0
2000–2010 (11 year)	10	10	4
2011–2022 (12 year)	11	14	6

underlying dynamics of the enhancement of the SAH differ from those of ordinary HWs.

b. Discussion

Hong et al. (2017) and Wang et al. (2017) documented the decadal modulation of the Silk Road pattern on asymmetric warming over East Asia. In addition, Li and Sun (2017) pointed out that the decadal variation in the Silk Road pattern can modulate the frequency of extreme hot days over the YRB. To further explore the decadal variation in the HWs and its relationship with the upper-level enhanced SAH, we identified the extremely strong SAH events via a similar method that is applied to the extreme HWs. The quantity utilized in the identification is the vertically averaged LWA anomalies from 7 to 17 km over eastern China [20–40° N, 90–120° E] (black rectangle in Fig. 7). Table 1 shows the numbers of extreme HWs, extreme LWA events and events that overlap between the two types of extreme events. Here, an overlapped event is defined as that the lifecycle of an extreme HW event and that of an extreme SAH event overlap for at least 2 days. Clearly, the numbers of extreme HWs show an evident decadal variation, with higher occurrence in the 1960s and the last two decades. Interestingly, extreme SAH events also exhibit a similar decadal variation, except for the 1970s. Approximately 39% of extreme HWs are accompanied by extreme SAH events in the first two decades, while this percentage has increased to approximately 48% in the last two decades. This suggests that the influences from upper-level circulation anomalies have become more pronounced in recent periods. Therefore, when analysing the formation of HWs, it is crucial to consider the impact of upper-level influences more than ever before. Further studies are needed to understand the underlying reasons for the decadal variation in the frequency of these extreme events.

Supplementary Information The online version contains supplementary material available at https://doi.org/10.1007/s00382-024-07104-6.

Author contributions All authors contributed to the study conception and design. Material preparation, data collection and analysis were performed by Wencai Liu and Ning Shi. Huijun Wang proposed the scientific questions, which inspired the writing of this article. Figures 1 and 2 and Table 1 were prepared by Qilei Huang. All authors commented on previous versions of the manuscript. And all the authors have read and approved the final manuscript.

Funding This work is jointly supported by the National Key R&D Program of China (No. 2022YFF0801601), the National Natural Science Foundation of China (No. 41975063) and the funding of Jiangsu innovation & entrepreneurship team.

Data availability The JRA-55 reanalysis data are available through the National Center for Atmospheric Research (USA): https://rda.ucar.edu/datasets/ds628.0/. The ERA5 reanalysis data are available at https://cds.climate.copernicus.eu/cdsapp#!/dataset/reanalysis-era5-single-levels-monthly means?tab = form. Figures were drawn using NCAR Command Language Version 6.6.2, which is available at http://www.ncl.ucar.edu/.

Declarations

Conflict of interest The authors have no relevant financial or nonfinancial interests to disclose.

References

Chen X, Zhou T (2018) Relative contributions of external SST forcing and internal atmospheric variability to July–August heat waves over the Yangtze River valley. Clim Dyn 51:4403–4419

Chen R, Wen Z, Lu R et al (2019) Causes of the extreme hot midsummer in Central and South China during 2017: role of the Western Tropical Pacific Warming. Adv Atmos Sci 36:465–478

Ding Q, Wang B (2005) Circumglobal teleconnection in the Northern Hemisphere Summer. J Clim 18:3483–3505

Fischer EM, Seneviratne SI, Vidale PL et al (2007) Soil moisture-atmosphere interactions during the 2003 European Summer Heat Wave. J Clim 20:5081–5099

Gao M, Wang B, Yang J et al (2018) Are peak summer sultry heat wave days over the Yangtze-Huaihe River basin predictable? J Clim 31:2185–2196

He C, Zhou T, Zhang L, et al (2023) Extremely hot East Asia and flooding western South Asia in the summer of 2022 tied to reversed flow over Tibetan Plateau. Clim Dyn 61:2103–2119

Hersbach H, Bell B, Berrisford P et al (2020) The ERA5 global reanalysis. Q J R Meteorol Soc 146:1999–2049

Hirschi M, Seneviratne SI, Alexandrov V et al (2011) Observational evidence for soil-moisture impact on hot extremes in southeastern Europe. Nat Geosci 4:17–21

Hong X, Lu R, Li S (2017) Amplified summer warming in Europe-West Asia and Northeast Asia after the mid-1990s. Environ Res Lett 12:094007

Hong H, Sun J, Wang H (2022) Variations in summer extreme high-temperature events over Northern Asia and the possible mechanisms. J Clim 35:335–357
Horton RM, Mankin JS, Lesk C et al (2016) A review of recent advances in research on extreme heat events. Curr Clim Change Rep 2:242–259
Huang R (1992) The East Asia/Pacific teleconnection pattern of summer circulation and climate anomaly in East Asia. Acta Meteorol Sin 6:25–37
Huang C, Nakamura N (2016) Local finite-amplitude wave activity as a diagnostic of anomalous weather events. J Atmos Sci 73:211–229
Huang C, Nakamura N (2017) Local wave activity budgets of the wintertime Northern Hemisphere: implication for the Pacific and Atlantic storm tracks. Geophys Res Lett 44:5673–5682
Jiang J, Liu Y, Mao J et al (2023) Extreme heatwave over Eastern China in summer 2022: the role of three oceans and local soil moisture feedback. Environ Res Lett 18:044025
Kobayashi S, Ota Y, Harada Y et al (2015) The JRA-55 reanalysis: general specifications and basic characteristics. J Meteorol Soc Jpn Ser II 93:5–48
Li R, Sun J (2017) Interdecadal variability of the large-scale extreme hot event frequency over the middle and lower reaches of the Yangtze River basin and its related atmospheric patterns. Atmos Ocean Sci Lett 11:63–70
Li J, Ding T, Jia X et al (2015) Analysis on the extreme heat wave over China around Yangtze River Region in the Summer of 2013 and Its Main Contributing Factors. Adv Meteorol 2015:706713
Liang P, Zhang Z, Ding Y, et al (2023) The 2022 extreme heatwave in Shanghai, lower reaches of the Yangtze River Valley: combined influences of multiscale variabilities. Adv Atmos Sci https://www.iapjournals.ac.cn/aas/en/article. https://doi.org/10.1007/s00376-023-3007-8
Liu B, Zhu C, Su J et al (2019) Record-breaking northwards shift of the Western North Pacific Subtropical High in July 2018. J Meteorol Soc Jpn Ser II 97:913–925
Liu B, Zhu C, Ma S, Yan Y, Jiang N (2023) Subseasonal processes of triple extreme heatwaves over the Yangtze River Valley in 2022. Weather Clim Extremes 40:100572
Lu R, Oh J, Kim B (2002) A teleconnection pattern in upper-level meridional wind over the North African and Eurasian continent in summer. Tellus 54A:44–55
Lu R, Xu K, Chen R et al (2023) Heat waves in summer 2022 and increasing concern regarding heat waves in general. Atmos Ocean Sci Lett 16:10. https://doi.org/10.1016/j.aosl.2022.100290
Ma S, Zhou T, Stone DA et al (2017) Attribution of the July–August 2013 heat event in Central and Eastern China to anthropogenic greenhouse gas emissions. Environ Res Lett. https://doi.org/10.1088/1748-9326/aa69d2
Mallapaty S (2022) China's extreme weather challenges scientists trying to study it. Nature 609:888
Miralles DG, Teuling AJ, van Heerwaarden CC et al (2014) Mega-heatwave temperatures due to combined soil desiccation and atmospheric heat accumulation. Nat Geosci 7:345–349
Nakamura N, Huang CSY (2018) Atmospheric blocking as a traffic jam in the jet stream. Science 361:42–47
Nitta T (1987) Convective activities in the tropical western Pacific and their impact on the northern hemisphere summer circulation. J Meteorol Soc Jpn 65:373–390
Peng J, Sun S, Lin D (2023) The extreme hot event along the Yangtze Basins in August 2022. J Appl Meteorol Sci 34(5):527–539 (**in Chinese**)
Rahmstorf S, Coumou D (2011) Increase of extreme events in a warming world. Proc Natl Acad Sci U S A 108:17905–17909
Ren L, Zhou T, Zhang W (2020) Attribution of the record-breaking heat event over Northeast Asia in summer 2018: the role of circulation. Environ Res Lett 15:054018
Röthlisberger M, Papritz L (2023) Quantifying the physical processes leading to atmospheric hot extremes at a global scale. Nat Geosci 16:210–216
Shi N, Wang Y, Wang X et al (2019) Interdecadal variations in the frequency of persistent hot events in boreal summer over midlatitude Eurasia. J Clim 32:5161–5177
Shi N, SuolangTajie TP et al (2020) Contrasting relationship between wintertime blocking highs over Europe-Siberia and temperature anomalies in the Yangtze River basin. Mon Weather Rev 148:2953–2970
Sun J (2012) Possible impact of the summer North Atlantic oscillation on extreme hot events in China. Atmos Oceanic Sci Lett 5:231–234
Sun J (2014) Record-breaking SST over mid-North Atlantic and extreme high temperature over the Jianghuai-Jiangnan region of China in 2013. Chin Sci Bull 59:3465–3470
Sun Y, Zhang X, Zwiers FW et al (2014) Rapid increase in the risk of extreme summer heat in Eastern China. Nat Clim Chang 4:1082
Sun Y, Song L, Yin H et al (2016) Human Influence on the 2015 extreme high temperature events in Western China. Bull Am Meteor Soc 97:S102–S106
Sun B, Wang H, Huang Y et al (2023) Characteristics and causes of the hot-day climate anomalies in China during Summer of 2022. Trans Atmos Sci 46(1):1–8 (**in Chinese**)
Tang S, Qiao S, Wang B, et al (2023) Linkages of unprecedented 2022 Yangtze River Valley heatwaves to Pakistan flood and triple-dip La Niña. npj Clim Atmos Sci 6:44
Trigo RM (2005) How exceptional was the early August 2003 heatwave in France? Geophys Res Lett 32:L10701
Wang B, Wu R, Fu X (2000) Pacific-East Asia teleconnection: How does ENSO affect East Asian climate? J Clim 13:1517–1536
Wang W, Zhou W, Li X, Wang X, Wang D (2016) Synoptic-scale characteristics and atmospheric controls of summer heat waves in China. Clim Dyn 46:2923–2941
Wang L, Xu P, Chen W et al (2017) Interdecadal variations of the Silk Road pattern. J Clim 30:9915–9932
Wang J, Chen Y, Tett SFB et al (2020) Anthropogenically driven increases in the risks of summertime compound hot extremes. Nat Commun 11:528
Wang Z, Luo H, Yang S (2023) Different mechanisms for the extremely hot central-eastern China in July–August 2022 from a Eurasian large-scale circulation perspective. Environ Res Lett 18:10. https://doi.org/10.1088/1748-9326/acb3e5
Wu Z, Zhang P, Chen H et al (2016) Can the Tibetan Plateau snow cover influence the interannual variations of Eurasian heat wave frequency? Clim Dyn 46:3405–3417
Xie S, Kosaka Y, Du Y et al (2016) Indo-western pacific ocean capacitor and coherent climate anomalies in post-ENSO summer: a review. Adv Atmos Sci 33:411–432
Xoplaki E, Gonzálezrouco JF, Luterbacher J et al (2003) Mediterranean summer air temperature variability and its connection to the large-scale atmospheric circulation and SSTs. Clim Dyn 20:723–739
Zhang J, Wu L (2011) Land-atmosphere coupling amplifies hot extremes over China. Chin Sci Bull 56:3328–3332
Zhang D, Chen L, Yuan Y et al (2023) Why was the heat wave in the Yangtze River valley abnormally intensified in late summer 2022? Environ Res Lett 18:034014
Zschenderlein P, Fink AH, Pfahl S et al (2019) Processes determining heat waves across different European climates. Q J R Meteorol Soc 145:2973–2989